5-8-2009

Coexistence and transition between Cassie and Wenzel state on pillared hydrophobic surface

Takahiro Koishi
University of Fukui, Japan

Kenji Yasuoka
Keio University

Shigenori Fujikawa
Keio University, Yokohama, Japan

Toshikazu Ebisuzaki
Ebisuzaki Computational Astrophysics Laboratory, RIKEN, Wako, Japan

Xiao Cheng Zeng
University of Nebraska-Lincoln, xzeng1@unl.edu

Published in *Proceedings of the National Academy of Sciences U.S.A.* **106** (2009), pp. 8435-8440; doi 10.1073/pnas.0902027106 http://ww.pnas.org/cgi/doi/10.1073/pnas.0902027106

Submitted February 24, 2009; accepted April 3, 2009; published online May 8, 2009. Edited for *PNAS* by Benjamin Widom, Cornell University, Ithaca, NY.

Coexistence and transition between Cassie and Wenzel state on pillared hydrophobic surface

Takahiro Koishi,[1,2] Kenji Yasuoka,[3] Shigenori Fujikawa,[2] Toshikazu Ebisuzaki,[4] and Xiao Cheng Zeng[5]

1 Department of Applied Physics, University of Fukui, 3-9-1 Bunkyo, Fukui 910-8507, Japan
2 Innovative Nanopatterning Research Laboratory, Keio University, Yokohama 223-8522, Japan
3 Department of Mechanical Engineering, Keio University, Yokohama 223-8522, Japan
4 Ebisuzaki Computational Astrophysics Laboratory, RIKEN, Wako, Saitama 351-0198, Japan
5 Department of Chemistry and Center for Materials and Nanoscience, University of Nebraska–Lincoln, Lincoln, NE 68588, USA
Corresponding author — X. C. Zeng, email xczeng@phase2.unl.edu

Abstract: Water droplets on rugged hydrophobic surfaces typically exhibit one of the following two states: (i) the Wenzel state [Wenzel RN (1936) *Ind Eng Chem* **28**:988–994] in which water droplets are in full contact with the rugged surface (referred as the wetted contact) or (ii) the Cassie state [Cassie, ABD, Baxter S (1944) *Trans Faraday Soc* **40**:546–551] in which water droplets are in contact with peaks of the rugged surface as well as the "air pockets" trapped between surface grooves (the composite contact). Here, we show large-scale molecular dynamics simulation of transition between Wenzel state and Cassie state of water droplets on a periodic nanopillared hydrophobic surface. Physical conditions that can strongly affect the transition include the height of nanopillars, the spacing between pillars, the intrinsic contact angle, and the impinging velocity of water nanodroplet ("raining" simulation). There exists a critical pillar height beyond which water droplets on the pillared surface can be either in the Wenzel state or in the Cassie state, depending on their initial location. The free-energy barrier separating the Wenzel and Cassie state was computed on the basis of a statistical-mechanics method and kinetic raining simulation. The barrier ranges from a few tenths of k_BT_0 (where k_B is the Boltzmann constant, and T_0 is the ambient temperature) for a rugged surface at the critical pillar height to ~8 k_BT_0 for the surface with pillar height greater than the length scale of water droplets. For a highly rugged surface, the barrier from the Wenzel-to-Cassie state is much higher than from Cassie-to-Wenzel state. Hence, once a droplet is trapped deeply inside the grooves, it would be much harder to relocate on top of high pillars.

Keywords: free-energy barrier, molecular dynamics simulation, nanodrop raining experiment, Wenzel-to-Cassie state transition

It is well known that microtextured or nanotextured hydrophobic surfaces can become superhydrophobic (1–39). In fact, nature provides first examples of superhydrophobic surfaces, such as lotus leaves and water striders' nonwetting legs (40–42). Synthetic microtextured surface structures like the lotus leaves have been fabricated to achieve high water repellency such that on these surfaces, water droplets are typically in the Cassie state (43) rather than the Wenzel state (44). In general, water droplets adhere more strongly to the textured surface in the Wenzel state than in the Cassie state, causing stronger contact-angle hysteresis. Hence, in many practical applications such as self-cleaning surfaces (6, 17), the Cassie state is preferred over the Wenzel state. It is also known that as the degree of surface roughness increases, the Cassie state becomes increasingly favorable compared with the Wenzel state. Hence, at certain degree of roughness, the Wenzel state and Cassie state can become more or less equally favorable and may even coexist on the same surface. From a statistical-mechanics point of view, the two states can coexist when they are separated by a high free-energy barrier by which one state is still metastable (free-energy local minimum), and the other is thermodynamically stable (free-energy global minimum). In this article, we present computer simulation evidence of coexisting Wenzel/Cassie state (or the bistable state) for water droplets on pillared hydrophobic surface. We have studied 4 conditions that affect the transition between the Wenzel and Cassie state: (i) The height of nanopillars, (ii) the spacing between pillars, (iii) the impinging velocity of water nanodroplet ("raining" effect), and (iv) the intrinsic contact angle of a droplet on the flat surface of the same material. For two special cases (when droplets are at the bistable state), we have computed free-energy barrier separating the Wenzel and Cassie state. This is a quantitative computation, at the molecular level, of the free-energy barrier between Wenzel and Cassie state of water nanodroplets.

The simulation system consists of a solid hydrophobic surface, either flat or rugged, and a nanodroplet of water. The flat surface assumes the structure of a (0001) graphite surface with hexagonally arranged atoms. In the molecular dynamics (MD) simulation (see "Materials and Methods"), atoms of the solid surface were fixed. The rugged surface is an artificial pillared surface. Quadrangular pillars with lateral size of 12.3 × 12.8 Å were arranged with spacing of 12.3/12.8 Å between them in the *x*/*y* direction. A larger spacing of 14.8/14.9 Å between pillars was also examined. This near-square-lattice pillar arrangement has been used previously by Lundgren et al. (11, 32). The height of nanopillars is adjustable, ranging from 2 graphite–interlayer distance (6.7 Å) to 30 interlayer distance (100.4 Å). For MD simulations with a larger water droplet, the initial configuration of water droplet is a 18 × 18 × 18 (5,832) molecules cube with a side length of 55.9 Å. This length scale was selected based on liquid water density of 0.997 g/cm3 at 298 K. The lateral size of the solid surface is 167.4 × 168.4 Å, ~3 times the length of the water cube. The length of the simulation cell (280 Å) is 5 times the length of the water cube. For MD simulations with a smaller water droplet, the initial configuration of the water droplet was a 12 × 12 × 12 (1,728) molecules cube; the lateral size of the solid surface is 110.8 × 110.8 Å, ~3 times the length of the smaller water cube.

Results and Discussion

To measure wettability of the model hydrophobic surfaces, we first computed the intrinsic contact angle of a water nanodroplet on the flat surfaces (11, 32, 45). To this end, we used the following computational approach to determine the surface locus of a water nanodroplet. We divided the entire simulation cell into many cubic meshes, each with length scale of 5 Å. The average local water density in each cubic mesh was recorded. Having obtained the local water density, we can identify the spatial points where the local density is half of the bulk water. The locus of these points gives rise to the surface of the droplet. The

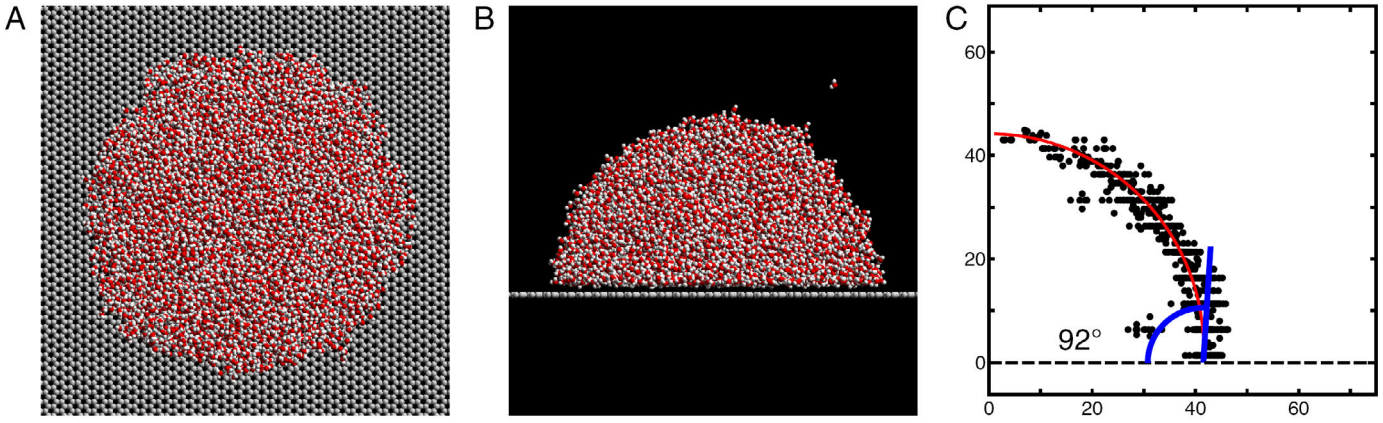

Figure 1. Measurement of the intrinsic contact angle of a flat surface. (A and B) Top **(A)** and side **(B)** views of a water nanodroplet on a flat solid hydrophobic surface. **(C)** Black points denote half-bulk-density points to characterize the surface of water nanodroplet, the red curve is a fit to black points, and the blue curve denotes the contact angle.

contact angle is defined as the angle between a tangential line of the droplet surface (described by a fitting circle) at any 3-phase contact point and the line in the flat surface. Note that both lines must be in the same plane through the center of the droplet. Snapshots of the water nanodroplet are shown in Figure 1 A and B and supporting information (SI) Figure S1. Depending on the interaction parameter between water molecule and atom of the solid surface (see "Materials and Methods"), the computed contact angles range from 92° to 127° (see Figure 1C and Figure S1). Hereafter, we will mainly focus on 2 weakly hydrophobic surfaces whose contact angles are ~92° and ~99°, respectively. Note that the contact angle of a graphite surface is ~85°.

Next, we performed MD simulations of the larger water nanodroplet on pillared surfaces to examine texture effects on the shape and location of the droplet. Two initial locations for the larger water cube were considered, one on top of the pillars (Figure 2, Ai–Di) and another at the bottom of the grooves (Figure 2, Ei–Hi). Here, the height of identical pillars ranges from 2 to 5 graphite–interlayer distance. Totally, 8 systems were studied, each equilibrated for 1 ns. Snapshots of the equilibrated droplet at t =1.0 ns for these systems are shown in Figure 2, Aii–Dii, and Eii–Hii. When the water cube is initially placed at the bottom of the grooves, the final state of the droplet is always the Wenzel state (Figure 2, Eii–Hii), regardless of the height of pillars. However, when the water cube is initially placed on top of the pillars, the final state is sensitive to the height of the pillars. When the height is 2 or 3 graphite–interlayer distance, the droplet still prefers the Wenzel state (Figure 2, Aii and Bii). But when the height is >4 graphite–interlayer distance (13.4 Å), the droplet adopts the Cassie state (here, the "air nanopockets" are essentially nanosized cavities between nanopillars). In other words, at low pillar height, the Wenzel state is the only stable state for the droplet. But when the height is beyond a critical value, e.g., 13.4 Å, the Cassie state is metastable, separated from the stable Wenzel state by a free-energy barrier (18, 23, 37). As such, coexistence of Wenzel and Cassie state for water droplets is possible, depending on the initial location of the droplets (18, 19, 23, 35–37).

At high pillar height, the transition from the metastable Cassie state to the stable Wenzel state becomes more difficult due to an increasingly higher free-energy barrier. To gain more insights into relative stability of the Cassie and Wenzel states, it is important to have quantitative values of the free-energy barrier that separates the Wenzel and Cassie state, as schematically shown in Figure 3 (23, 37). To this end, we used two computer simulation methods: one kinetic and one equilibrium. The kinetic method is basically a computer experiment of nanodroplet "raining," namely, a water droplet impinging the pillared surface. This raining simulation mimics macroscopic raining experiments (recently reported for designing micropatterned superhydrophobic surfaces) (28, 29). Besides the design of nanopatterned surfaces, the raining simulation allows quantitative evaluation of the free-energy barrier through preparation of water droplets with exactly the same number of molecules and impurity-free (perfectly dry) surfaces. Specifically, a water droplet was initially located 60 Å from the top of pillars (Figure 4A) and was equilibrated there for 200 ps at T_0 = 298 K, where $T_0 = (3N_fK_B)^{-1} \sum_{i=1}^{N} m_w(v_{ix}^2 + v_{iy}^2 + v_{iz}^2)$, N is the number of water molecules, N_f is the total degrees of freedom, m_w is the mass of a water molecule, k_B is the Boltzmann's constant, and v_{ix}, v_{iy}, and v_{iz} are the x, y, and z velocity component of water molecule i. At time t_1 = 200 ps, a downward velocity v_d was imposed instantly to all water molecules such that z component of the velocity of water molecule i became v'_{iz} (= v_{iz} (t_1) + v_d). Before the droplet colliding with the surface, the velocity components (v'_{ix}, v'_{iy}, and v'_{iz}) always satisfy the conditions that the system-averaged velocities $\langle v'_{ix} \rangle = 0$, $\langle v'_{iy} \rangle = 0$, and $\langle v'_{iz} \rangle = v_d$, and the constraint that the temperature T_0 = 298 K. After the droplet collided with the pillared surface and eventually settled down either on top of the pillars (Cassie state) or at the bottom of the grooves (Wenzel state), the system-averaged velocities satisfy $\langle v'_{ix} \rangle = 0$, $\langle v'_{iy} \rangle = 0$, and $\langle v'_{iz} \rangle = 0$.

The downward velocity v_d was carefully chosen to attain sufficient number of statistical events for both the Cassie and Wenzel states (Figure 4, B and C; also see Movie S1 and Movie S2). If v_d is too high, the water droplet can easily go over the free-energy barrier and reaches the Wenzel state. If v_d is too low, the water droplet favors the Cassie state. In the first raining experiment, we performed 926 totally independent MD simulations and recorded the number of events for the droplet in the Wenzel or Cassie state. Nine selected downward velocities and the number of MD runs for each given v_d are listed in Table 1. The probability for the droplet in the Wenzel state P_w was computed (for each given v_d) and shown in Table 1. The probability P_w can be fitted to an exponential equation

$$P_w = P_0 \exp(-\Delta G_{cw}/e_k), \quad [1]$$

where P_0 is a preexponential factor, G_{cw} is defined as the free-energy barrier from the Cassie to Wenzel state, and e_k is the ki-

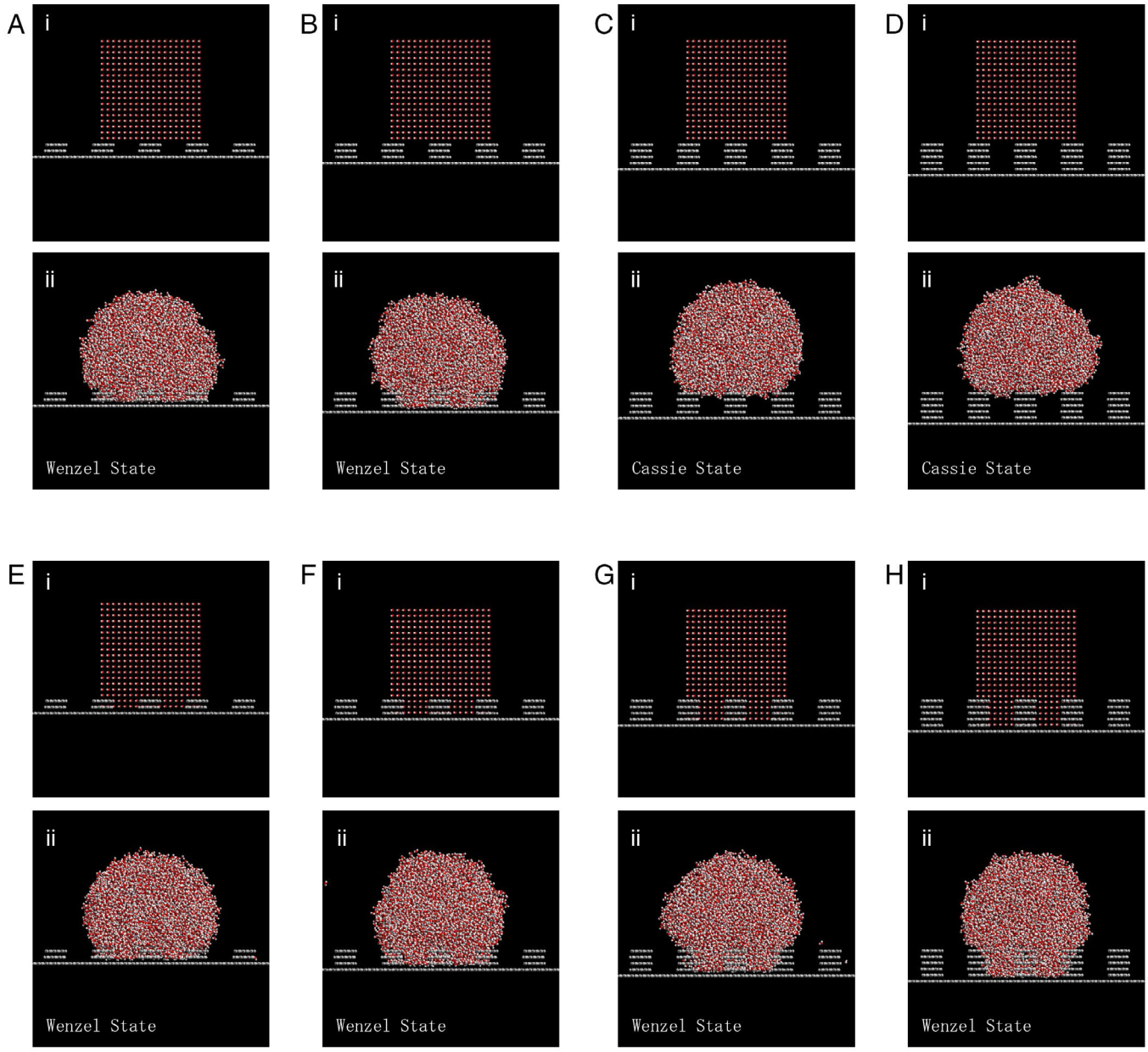

Figure 2. Simulation of a water nanodroplet on various pillared hydrophobic surfaces. **(Ai–Hi)** Initial configurations of the water cube (with 5,832 water molecules) on top of the pillars **(Ai–Di)** and at bottom of the groove **(Ei–Hi)**. **(Aii–Dii & Eii–Hii)** Snapshots of the corresponding system at t = 1.0 ns.

netic energy of the center of mass of the droplet (per molecule), given by

$$e_k = \tfrac{1}{2}\, m_w\, v_d^2 . \qquad [2]$$

In Figure 5, a fit to numerical probabilities P_w vs. e_k (filled circles) to the natural logarithm of Equation 1 gives rise to a free-energy barrier of ΔG_{cw} = 0.334 kJ/mol ≈ 0.135 $k_B T_0$. This barrier corresponds to the condition that the height of pillars is at the critical value of 13.4 Å. In the second computer experiment, we used the smaller water droplet (with 1,728 water molecules) but otherwise the same pillared surface. After 816 independent MD simulations (102 MD runs for each given downward v_d), we obtained the free-energy barrier of ΔG_{cw} = 0.328 kJ/mol ≈ 0.132 $k_B T_0$, very close to the barrier of ΔG_{cw} = 0.334 kJ/mol. These results indicate that the free-energy barrier is not very sensitive, to some extent, to the size of water droplet. In the third computer experiment, we still used the smaller water droplet but a larger spacing between pillars, that is 14.8/14.9 Å in the x/y direction. Totally, 810 independent MD simulations were carried out. The obtained free-energy barrier is ΔG_{cw} = 0.00286 kJ/mol, considerably lower than the barrier of ΔG_{cw} = 0.328 kJ/mol. This indicates that the spacing between pillars has a profound effect on the stability of the metastable Cassie state. In the fourth computer experiment, we used the same simulation system as in the second computer experiment but the pillared surface has a larger intrinsic contact angle of 99°. Totally, 773 independent MD simulations were carried out. The numerical probabilities P_w and kinetic energy of the droplet e_k (open circles) are shown in Figure 5. After fitting the data to Equation 1, we obtained a free-energy barrier of ΔG_{cw} = 1.41 kJ/mol ≈ 0.57 $k_B T_0$. This barrier is appreciably higher than ΔG_{cw} = 0.328 kJ/mol, indicating that the intrinsic contact angle can also strongly affect the stability of the Cassie state.

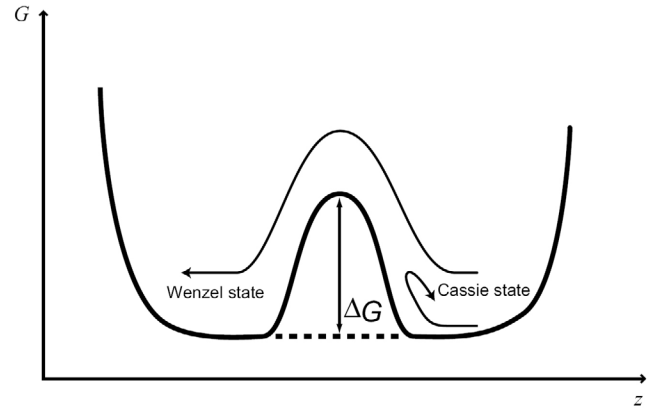

Figure 3. A schematic plot of the free-energy barrier ΔG, separating the Wenzel and Cassie state.

Finally, we computed the free-energy barrier for a system with very high pillar height whose length scale is greater than length scale of the water droplet. In this case, the raining experiment is not effective to compute the free-energy barrier because the water droplet would overwhelmingly favor the Cassie state. We therefore invoke a statistical-mechanics method to evaluate the free-energy barrier. We still used the larger droplet (with 5,832 water molecules) and the pillared surface with an intrinsic contact angle of 92°, but the height of the pillars amounts to 100.4 Å. The water cube was placed at two initial positions: (i) an upper position but not fully embedded by the pillars, or (ii) a lower position where the entire water cube is embedded in the groove region, as shown in Figure 6, A and D. The system was then relaxed to achieve equilibration. Interestingly, the water cube at the upper position ascended upward and turned to a spherical-like droplet on top of the high pillars (Figure 6, B and C, and Movie S3]. We found that as long as a small portion of water cube is above the top of the pillars, the water cube always ascends to the top of the pillars. On the other hand, the water cube at the lower position tends to descend toward the bottom of the grooves (Figure 6, E and F). We performed 210 independent MD simulations, 105 each for the droplet ascending and descending. The free-energy barrier ΔG_1 can be computed by taking an integration of the position- dependent z component of the total force, $f_z(z)$, acting on entire water droplet, that is,

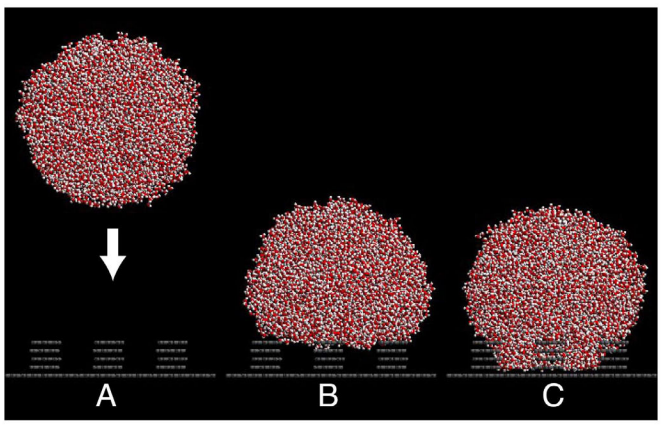

Figure 4. A snapshot of a water droplet (with 5,832 water molecules) at constrained equilibrium state above the pillars **(A)**, the Cassie state **(B)**, or the Wenzel state **(C)** after the droplet collided with the pillared surface.

Table 1. Calculated probability P_w of the Wenzel state, given different downward velocity v_d of the droplet (with 5,832 water molecules)

vd, m/s	e_k, kJ/mol	Cassie	Wenzel	P_w
118	0.125	82	20	0.196
129	0.150	71	32	0.311
136	0.167	79	24	0.233
140	0.176	63	40	0.388
155	0.215	51	51	0.500
169	0.256	33	69	0.676
176	0.278	23	79	0.775
183	0.301	19	83	0.814
190	0.324	18	84	0.824

$$\Delta G_1 = \int_{z_0}^{z} \langle f_z(z) \rangle \, dz, \qquad [3]$$

where z_0 is the initial position of the center of mass of the droplet. The trajectory of averaged z coordinate of the center of mass of the droplet is shown in Figure 7A. The integration of $f_z(z)$ is plotted in Figure 7B. The minimum at the upper equilibrium position ($z \approx 127.4$ Å) gives rise to a free-energy barrier of $\Delta G_{cw} = 4.83$ kJ/mol $\approx 1.9\ k_B T_0$. This barrier is an order of magnitude higher than that (0.334 kJ/mol) in the case of low-pillar surface, indicating the strong effect of the pillar height to the stability of the metastable Cassie state. On the other hand, the minimum at the lower equilibrium position ($z \approx 28$ Å) gives rise to a free-energy barrier of $\Delta G_{wc} = 18.6$ kJ/mol $\approx 7.5\ k_B T_0$ (from the Wenzel-to-Cassie state), indicating that once a droplet is trapped in the groove region, it would be much harder for it to reach to the top of high pillars because the Wenzel state is the thermodynamically stable state.

Conclusion

We present a simulation evidence of coexisting Wenzel/Cassie state for water droplets on a pillared hydrophobic surface. There generally exists a critical pillar height beyond which water droplets on pillared hydrophobic surfaces can be in the bistable Wenzel/Cassie state, depending on the initial location of the droplets. More importantly, the free-energy barrier

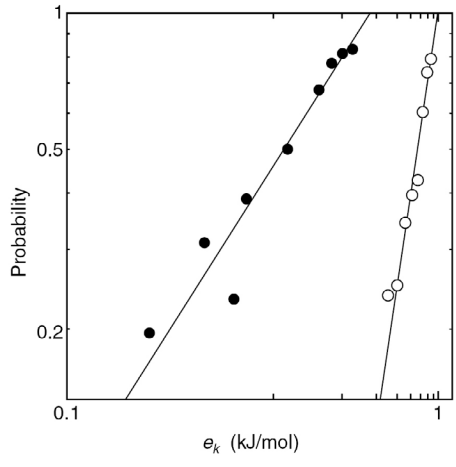

Figure 5. A straight-line fit to computed probability P_w (at the Wenzel state) and kinetic energy of the center of mass of (i) the larger droplet with 5,832 water molecules (filled circles) and (ii) the smaller droplet with 1,728 water molecules (open circles). The larger droplet collided with the pillared surface with intrinsic contact angle of 92°, whereas the smaller droplet collided with the pillared surface with intrinsic contact angle of 99°.

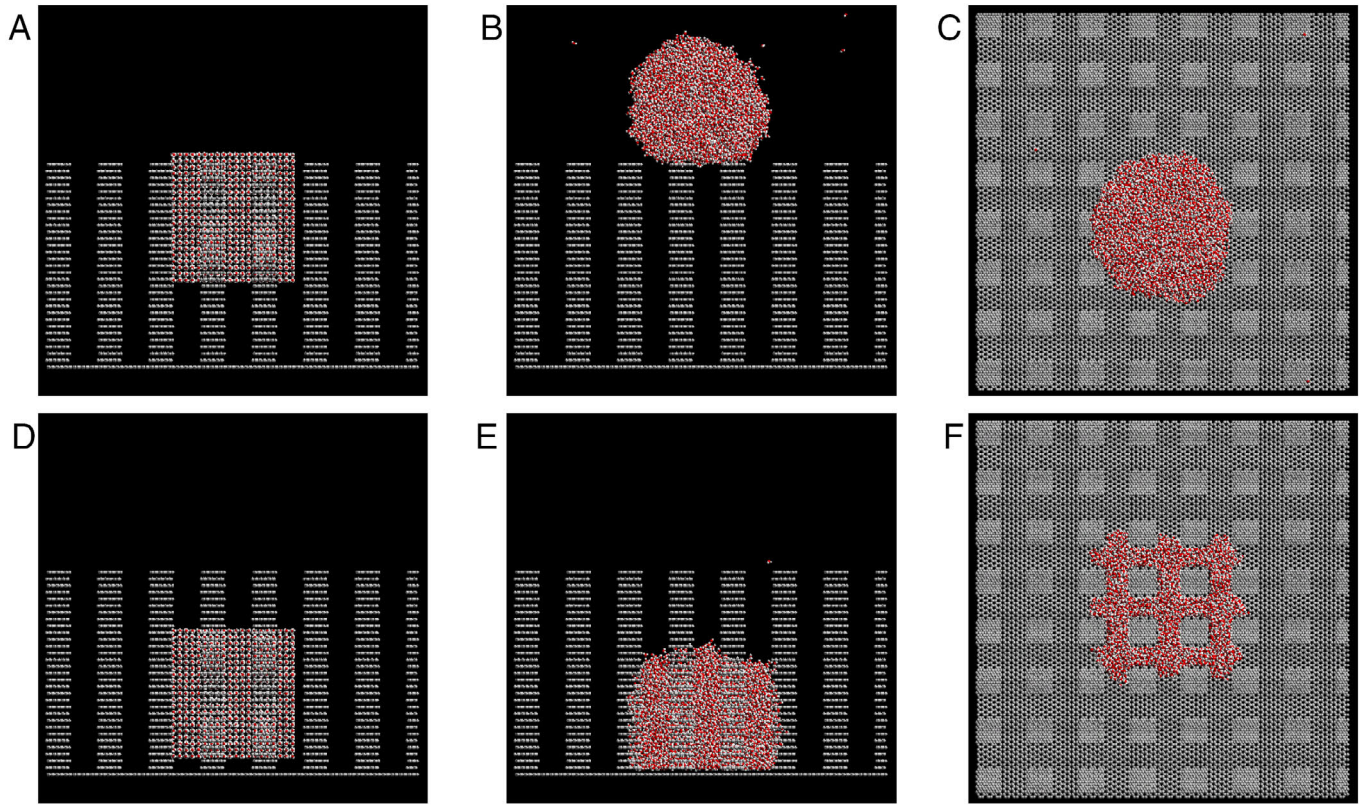

Figure 6. Side view of two initial configurations (**A** and **D**) of the system; side view (**B** and **E**), and top view (**C** and **F**) of a snapshot of the equilibrium state of the system. The water droplet has 5,832 water molecules. The pillared surface has an intrinsic contact angle of 92°.

separating the Wenzel and Cassie states is computed on the molecular level, based on both raining experiments and a statistical-mechanics method. Typically, the barrier ranges from a few tenths of $k_B T_0$ for a pillared surface at the critical pillar height to ~8 $k_B T_0$ for a pillared surface with pillar height greater than the size of the water droplet. Knowledge on the dependence of the free-energy barrier to the pillar height, the spacing between pillars, and the intrinsic contact angle will benefit the future design of nanopatterned hydrophobic surfaces and practical applications in nanofluidics.

Materials and Methods

The MD simulation was carried out at a constant-volume and constant-temperature (298 K) condition. The temperature was controlled by using the velocity scaling method. The periodic boundary condition was applied in all 3 spatial dimensions. The *z* dimension of the simulation cell (perpendicular to the pillared surface) is sufficiently large to avoid direct interaction between the water droplet and periodic images of pillared surfaces. A rigid-body model of water, the SPC/E (46) model, was used. The potential function of the SPC/E model includes two terms, a Coulomb term and a Lennard–Jones (LJ) term. The long-range charge–charge interaction between water molecules was calculated by using the Ewald method. Atoms of the flat and pillared surfaces were simply as-

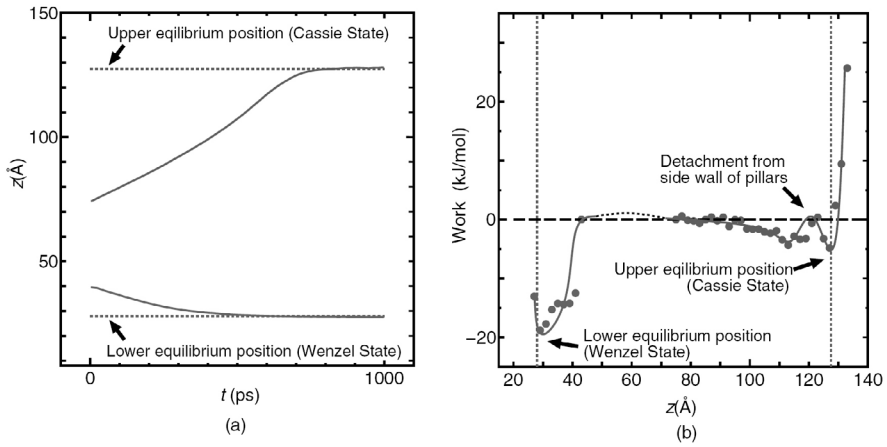

Figure 7. (a) Time dependence of the *z* coordinate of the center of mass of the water droplet starting from two different initial locations (Figure 6, A and D). **(b)** The mechanical work done on the droplet by the pillared surface is used to characterize the free-energy barrier separating the minima of the Wenzel (left-side curve) and Cassie (right-side curve) states. A small hump at *z* = 120 Å is due to the work required to detach the droplet from the side walls of pillars near the top of the pillars (see Figure S2).

sumed to be LJ particles whose size and energy parameters are σ = 3.4 Å and ε = 0.2325 kJ/mol, respectively (47). The hydrophobicity of the solid surfaces can be adjusted by multiplying a parameter (in the range of 0.5–1) and ε (see Figure S1). The time integration for the translational and rotational motion was undertaken by using the velocity Verlet method and time-reversible algorithm (48). The MD time step was set at 2.0 fs. In the initial MD simulation, translational motion of water molecules was not involved for 2.0 ps so that only orientational degrees of freedom of water molecules were relaxed.

Because of large number of simulations and a few very large system sizes involved in some simulations, we used a special-purpose computer "MDGRAPE-3" (49–51) to perform the MD simulations. The MDGRAPE-3 chips handle 3 force calculations: (i) the real-space part of the long-range charge–charge interaction, (ii) the van der Waals interaction, and (iii) the reciprocal-space part of long-range charge–charge interaction. Other computationally less-intensive calculations are handled by a host computer, which include updating particle positions and evaluating temperature. The special-purpose computer contains 1 MDGRAPE-3 board that consists of 12 MDGRAPE-3 chips. The peak performance of a MDGRAPE-3 board at 250 MHz is 2.16 TFLOPS. We used 2 special-purpose computers for the MD simulations; one for the real part of the Ewald calculation and another for the reciprocal-space part of Ewald calculation.

Acknowledgments — We are grateful for valuable discussions with Prof. Peter Rossky. This work was supported by the Japan Science and Technology Corporation, the Ministry of Education, Culture, Sport and Technology in Japan, and the Grant-in-Aid (KAKENHI) for Young Scientists (B). X. C. Z. was supported by U.S. Department of Energy Grant DE-FG02-04ER46164, National Science Foundation Grant CHEM-0427746, and by the Nebraska Research Initiative.

Author contributions: T.K., K.Y., S.F., and X.C.Z. designed research; T.K., K.Y., and X.C.Z. performed research; T.K., K.Y., S.F., and T.E. contributed new reagents/analytic tools; T.K., K.Y., and X.C.Z. analyzed data; and T.K. and X.C.Z. wrote the paper.

Supporting figures S1 and S2 and stills from Movies M1–M3 follow the References; AVI movie files are attached to the archive cover page for this article as "Additional files." These materials can also be found online at www.pnas.org/cgi/content/full/0902027106/DCSupplemental

References

1. Adam NK (1930) *The Physics and Chemistry of Surfaces* (Clarendon, Oxford, UK), pp 181–182.
2. Shuttleworth R, Bailey GLJ (1948) The spreading of a liquid over a rough solid. *Discuss Faraday Soc* **3**:16–22.
3. Onda T, Shibuichi S, Satoh N, Tsujii K (1996) Super-water-repellent fractal surfaces. *Langmuir* **12**:2125–2127.
4. Nakajima A, Fujishima A, Hashimoto K, Watanabe T (1999) Preparation of transparent superhydrophobic boehmite and silica films by sublimation of aluminum acetylacetonate. *Adv Mater* **11**:1365–1368.
5. Chen W, et al. (1999) Ultrahydrophobic and ultralyophobic surfaces: Some comments and examples. *Langmuir* **15**:3395–3399.
6. Nakajima A, et al. (2000) Transparent superhydrophobic thin films with self-cleaning properties. *Langmuir* **16**:7044–7047.
7. Tadanaga K, Morinaga J, Matsuda A, Minami T (2000) Superhydrophobic-superhydrophilic micropatterning on flowerlike alumina coating film by the sol-gel method. *Chem Mater* **12**:590–592.
8. Feng L, et al. (2002) Super-hydrophobic surfaces: From natural to artificial. *Adv Mater* **14**:1857–1860.
9. Wu Y, Sugimura H, Inoue Y, Takai O (2002) Thin films with nanotextures for transparent and ultra water-repellent coatings produced from trimethylmethoxysilane by microwave plasma CVD. *Chem Vapor Deposition* **8**:47–50.
10. Wagner P, Furstner R, Barthlott W, Neinhuis C (2003) Quantitative assessment to the structural basis of water repellency in natural and technical surfaces. *J Exp Bot* **54**:1295–1303.
11. Lundgren M, Allan NL, Cosgrove T, George N (2003) Molecular dynamics study of wetting of a pillar surface. *Langmuir* **19**:7127–7129.
12. Marmur A (2003) Wetting on hydrophobic rough surfaces: to be heterogeneous or not to be? *Langmuir* **19**:8343–8348.
13. Feng L, et al. (2003) Creation of a superhydrophobic surface from an amphiphilic polymer. *Angew Chem Int Ed* **42**:800–802.
14. Patankar NA (2003) On the modeling of hydrophobic contact angles on rough surfaces. *Langmuir* **19**:1249–1253.
15. He B, Patankar NA, Lee J (2003) Multiple equilibrium droplet shapes and design criterion for rough hydrophobic surfaces. *Langmuir* **19**:4999–5003.
16. Erbil HY, Demirel AL, Avci, Y, Mert O (2003) Transformation of a simple plastic into a superhydrophobic surface. *Science* **299**:1377–1380.
17. Blossey R (2003) Self-cleaning surfaces—Virtual realities. *Nat Mater* **2**:301–306.
18. Lafuma A, Quéré D (2003) Superhydrophobic states. *Nat Mater* **2**:457–460.
19. Patankar NA (2004) Transition between superhydrophobic states on rough surfaces. *Langmuir* **20**:7097–7102.
20. Jopp J, Grull H, Yerushalmi-Rozen R (2004) Wetting behavior of water droplets on hydrophobic microtextures of comparable size. *Langmuir* **20**:10015–10019.
21. Fan J-G, Tang X-J, Zhao Y-P (2004) Water contact angles of vertically aligned Si nanorod arrays. *Nanotechnology* **15**:501–504.
22. Narhe RD, Beysens DA (2004) Nucleation and growth on a superhydrophobic grooved surface. *Phys Rev Lett* **93**:076103/1–4.
23. Ishino C, Okumura K, Quéré D (2004) Wetting transitions on rough surfaces. *Europhys Lett* **68**:419–425.
24. Cheng Y-T, Rodak DE (2005) Is the lotus leaf superhydrophobic? *Appl Phys Lett* **86**:144101/1–3.
25. Hosono E, Fujihara S, Honma I, Zhou H (2005) Superhydrophobic perpendicular nanopin film by the bottom-up process. *J Am Chem Soc* **127**:13458–13459.
26. Guo Z, Zhou F, Hao J, Liu W (2005) Stable biomimetic super-hydrophobic engineering materials. *J Am Chem Soc* **127**:15670–15671.
27. Carbone G, Mangialardi L (2005) Hydrophobic properties of a wavy rough substrate. *Eur Phys J E* **16**:67–76.
28. Bartolo D, et al. (2006) Bouncing or sticky droplets: Impalement transitions on super- hydrophobic micropatterned surfaces. *Europhys Lett* **74**:299–305.
29. Reyssat M, Pe´ pin A, Marty F, Chen Y, Quéré D (2006) Bouncing transition on micro- textured materials. *Europhys Lett* **74**:306–312.
30. Yang C, Tartaglino U, Persson BNJ (2006) Influence of surface roughness on superhydrophobicity. *Phys Rev Lett* **97**:116103/1–4.
31. Krupenkin TN, et al. (2007) Reversible wetting–dewetting transitions on electrically tunable superhydrophobic nanostructured surfaces. *Langmuir* **23**:9128–9133.
32. Lundgren M, Allan NL, Cosgrove T (2007) Modeling of wetting: A Study of nanowetting at rough and heterogeneous surfaces. *Langmuir* **23**:1187–1194.
33. Barbieri L, Wagner E, Hoffmann P (2007) Water wetting transition parameters of perfluorinated substrates with periodically distributed flat-top microscale obstacles. *Langmuir* **23**:1723–1734.
34. Tuteja A, et al. (2007) Designing superoleophobic surfaces. *Science* **318**:1618–1622.
35. Moulinet S, Bartolo D (2007) Life and death of a fakir droplet: Impalement transitions on superhydrophobic surfaces. *Eur Phys J E* **24**:251–260.
36. Reyssat M, Yeomans JM, Quéré D (2008) Impalment of fakir drops. *Europhys Lett* **81**:26006/p1–p5.
37. Kusumaatmaja H, Blow ML, Dupuis A, Yeomans JM (2008) The collapse transition on superhydrophobic surfaces. *Europhys Lett* **81**:36003/p1–p6.
38. Gao L, Fadeev AY, McCarthy TJ (2008) Superhydrophobicity and contact-line issues. *Mater Res Soc Bull* **33**:747–751.
39. Tuteja A, Choi W, McKinley GH., Cohen RE, Rubner MF (2008) Design parameters for superhydrophobicity and superoleophobicity. *Mater Res Soc Bull* **33**:752–758.
40. Neinhuis C, Barthlott W (1997) Characterization and distribution of water-repellent, self-cleaning plant surfaces. *Ann Bot* **79**:667–677.
41. Gao X, Jiang L (2004) Biophysics: Water-repellent legs of water striders. *Nature* **432**:36.
42. Genzer J, Marmur A (2008) Biological and synthetic self-cleaning surfaces. *Mat Res Soc Bull* **33**:742–746.
43. Wenzel RN (1936) Resistance of solid surfaces to wetting by water. *Ind Eng Chem* **28**:988–994.
44. Cassie ABD, Baxter S (1944) Wettability of porous surfaces. *Trans Faraday Soc* **40**:546– 551.
45. Giovambattista N, Debenedetti PG, Rossky PJ (2007) Effect of surface polarity on water contact angle and interfacial hydration structure. *J Phys Chem B* **111**:9581–9587.
46. Beredensen HJC, Grigera JR, Straatsma TP (1987) The missing term in effective pair potentials. *J Phys Chem* **91**:6269–6271.
47. Bhethanabotla VR, Steele WA (1987) Molecular dynamics simulations of oxygen monolayers on graphite. *Langmuir* **3**:581–587.
48. Matubayasi N, Nakahara M (1999) Reversible molecular dynamics for rigid bodies and hybrid Monte Carlo. *J Chem Phys* **110**:3291–3301.
49. Taiji M, et al. (2003) Protein explorer: A petaflops special-purpose computer system for molecular dynamics simulations. *Proc ACM/IEEE SC2003* (High Performance Networking and Computing). doi 10.1109/SC.2003.10017
50. Taiji, M (2004) MDGRAPE-3 chip: A 165-Gflops application-specific LSI for molecular dynamics simulations. http://www.hotchips.org/archives/hc16
51. Narumi T, et al. A 55 TFLOPS simulation of amyloid-forming peptides from yeast prion Sup35 with the special-purpose computer system MDGRAPE-3. (2006) *Proc ACS/IEEE SC2006* (High Performance Computing, Networking, Storage and Analysis). http://doi.acm.org/10.1145/1188455.1188506

Supporting figures:

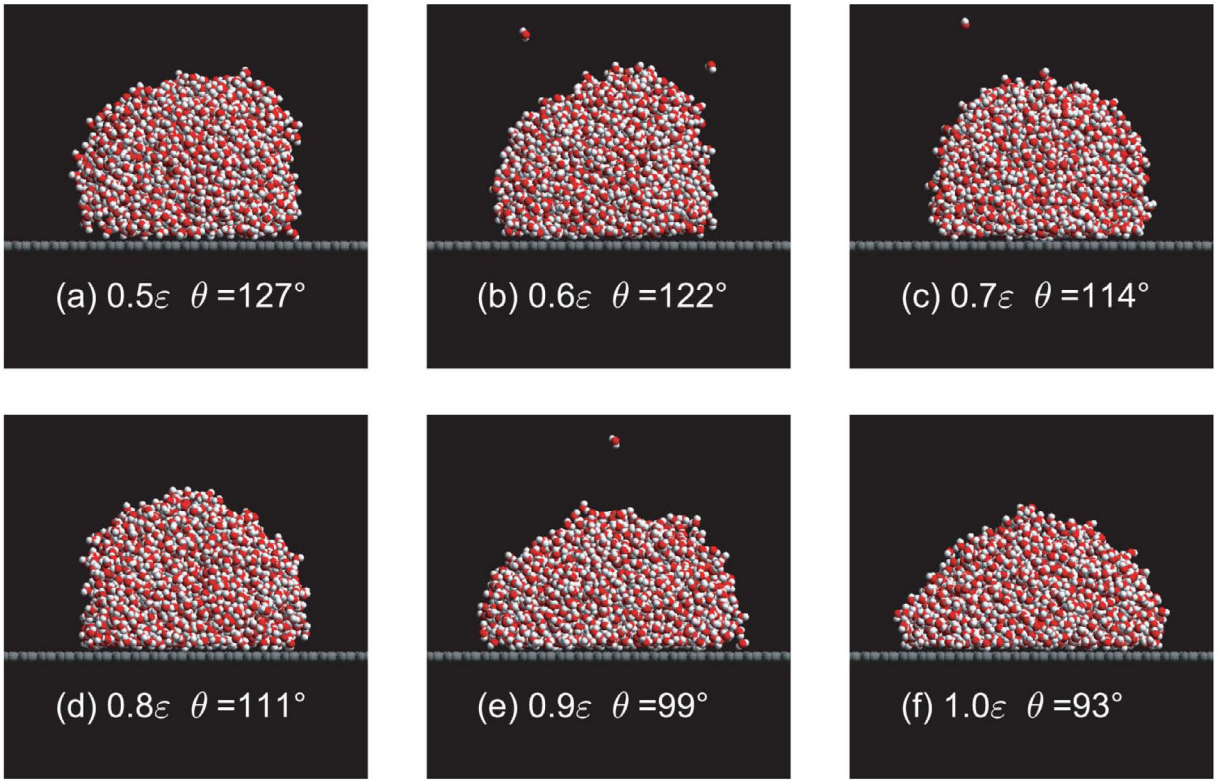

Figure S1. (**A–F**) Snapshots of a water nanodroplet on a flat solid hydrophobic surface. The hydrophobicity of solid surfaces can be adjusted by multiplying a parameter (in the range of 0.5–1) and the energy parameter of solid atoms, ε (see "Materials and Methods"). θ is the computed intrinsic contact angle of the flat solid surface.

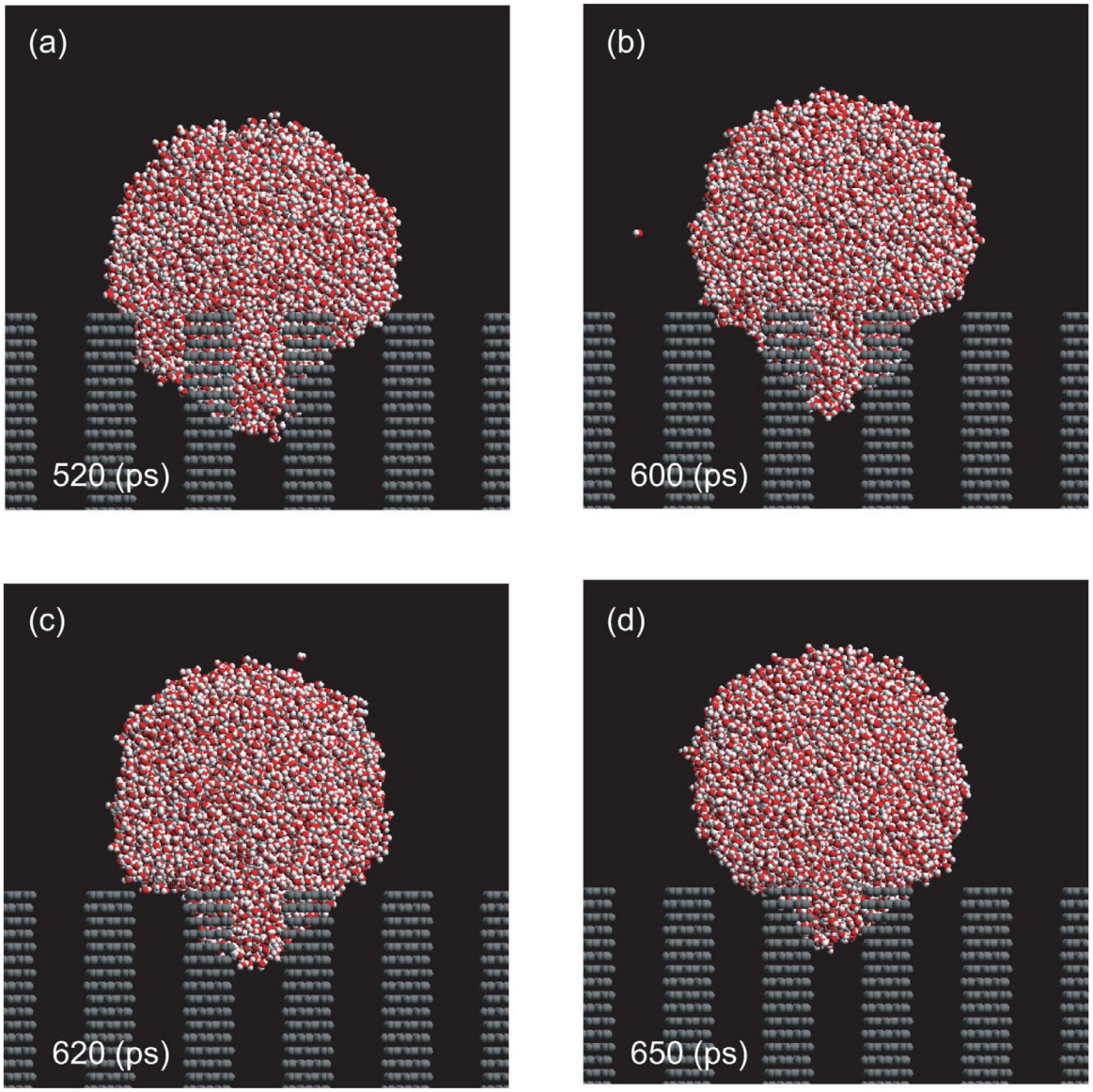

Figure S2. (**A–D**) A snapshot of a water nanodroplet on a pillared surface at MD simulation times of 520, 600, 620, and 650 ps, respectively. During this period, the droplet is about to detach from the side walls of the pillars while on the way to the top of the pillars.

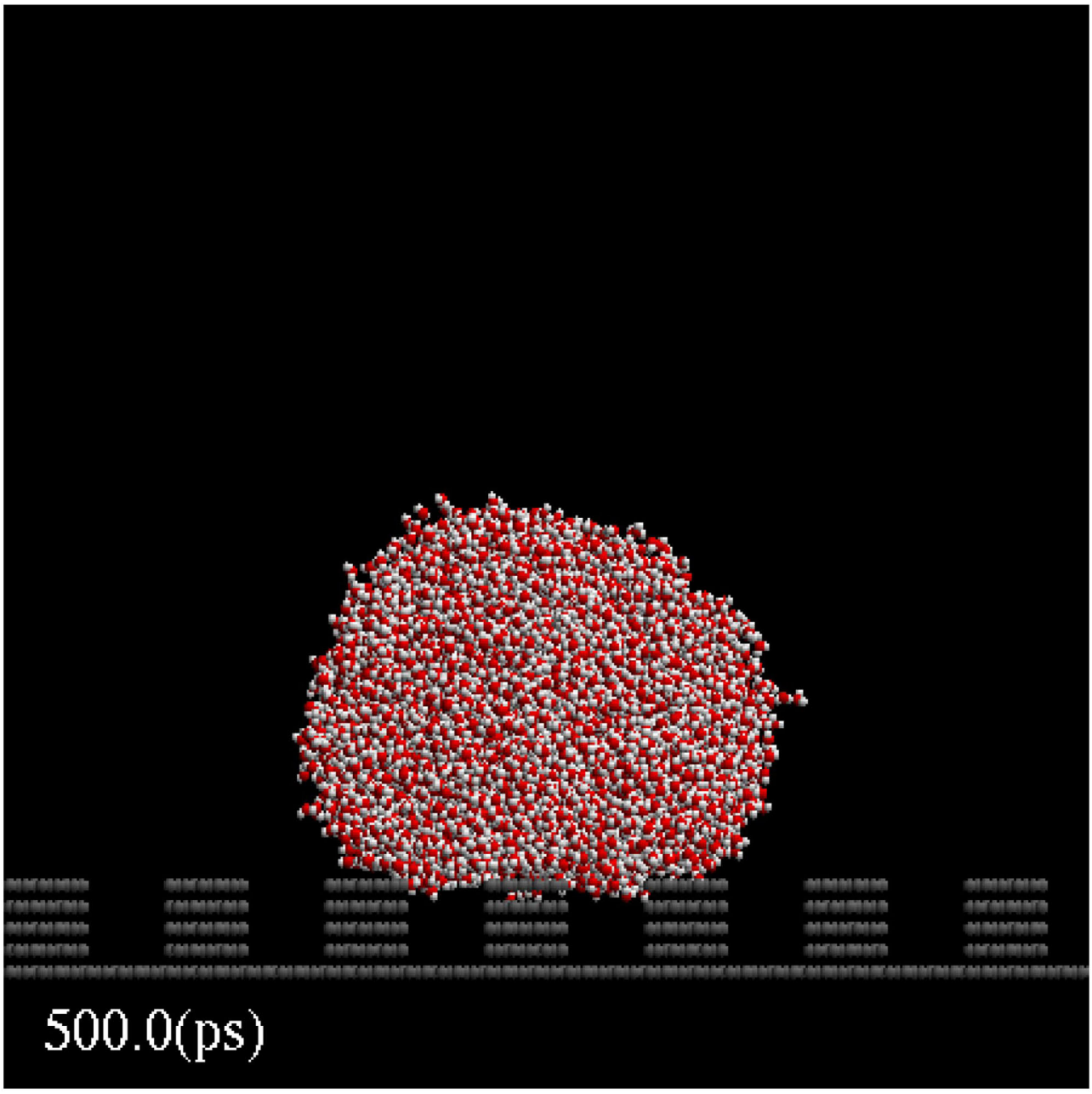

Movie S1. MD computer experiment of nanodroplet "raining," where a relatively low-speed water nanodroplet collides with a pillared surface. The final state of the nanodroplet is the Cassie state.

AVI movie files are attached to the archive cover page for this article as "Additional files."

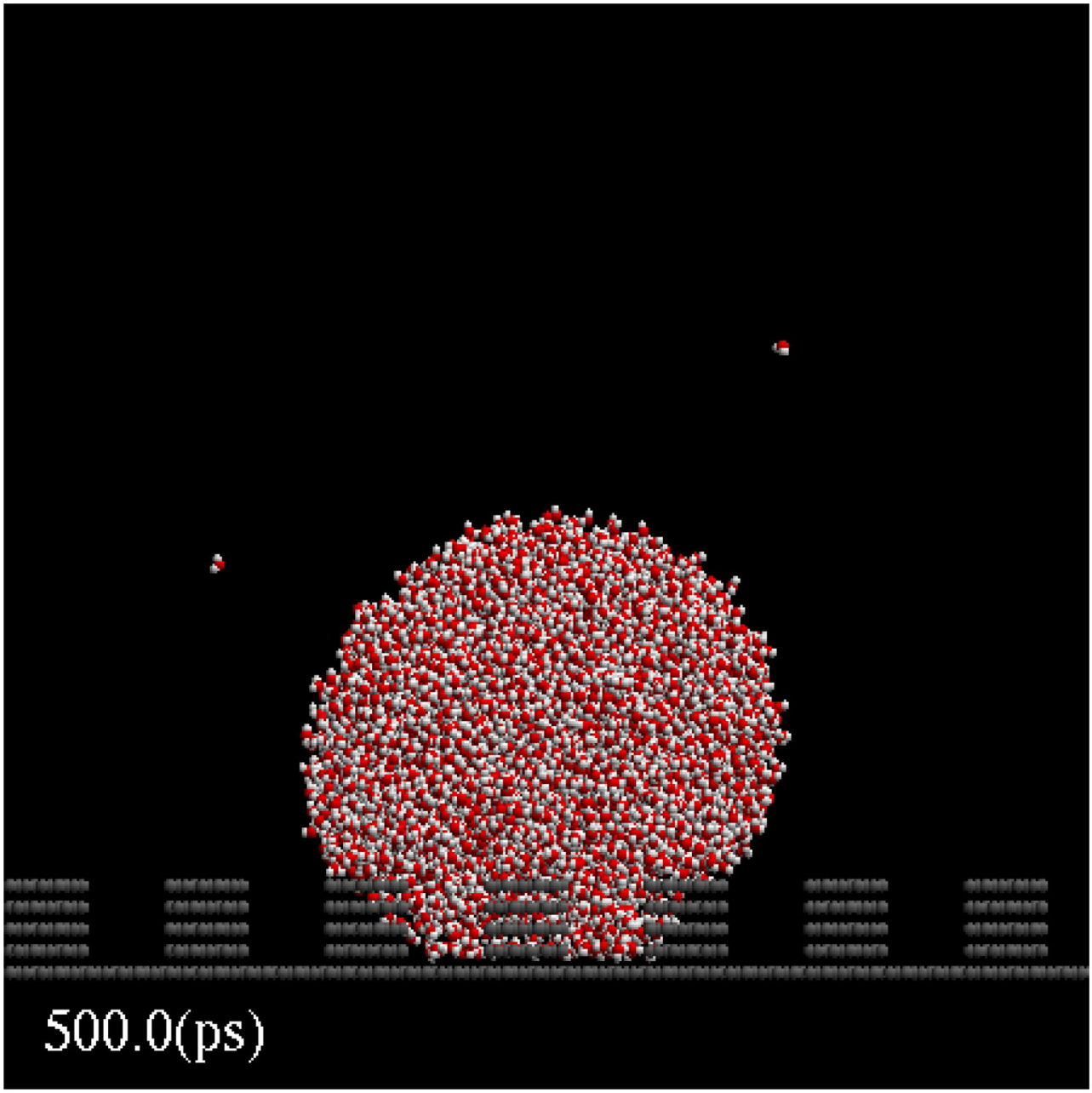

Movie S2. MD computer experiment of nanodroplet "raining," where a relatively high-speed water nanodroplet collides with a pillared surface. The final state of the nanodroplet is the Wenzel state.

AVI movie files are attached to the archive cover page for this article as "Additional files."

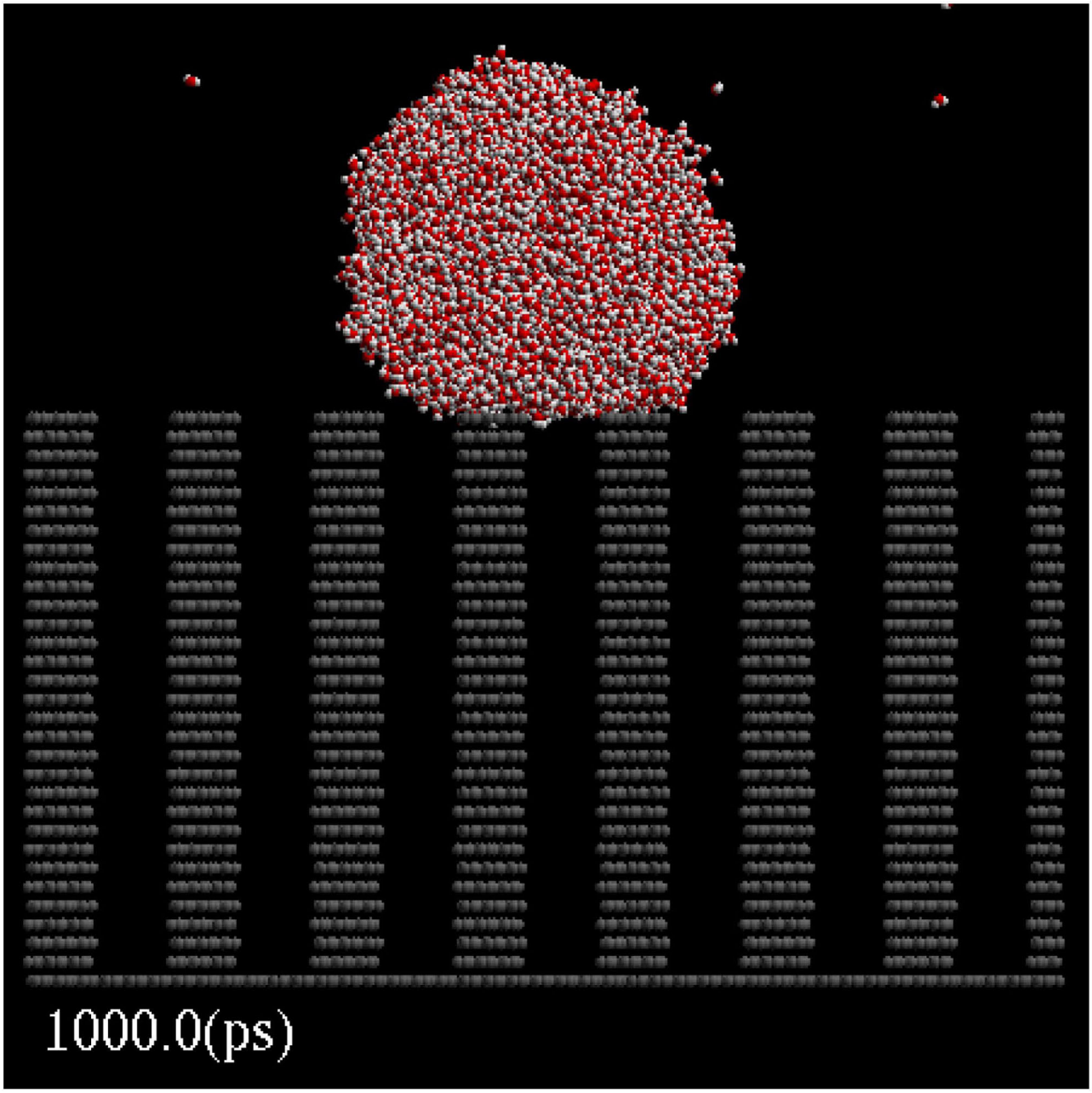

Movie S3. MD computer experiment, where a water nanodroplet was initially inserted into grooves of a pillared surface. The final state of the nanodroplet is the Cassie state.

AVI movie files are attached to the archive cover page for this article as "Additional files."